

## Supporting Information

### **The Influence of Elastic Strain on Catalytic Activity in the Hydrogen Evolution Reaction**

*Kai Yan, Tuhina Adit Maark, Alireza Khorshidi, Vijay A. Sethuraman, Andrew A. Peterson,\* and Pradeep R. Guduru\**

ange\_201508613\_sm\_miscellaneous\_information.pdf

# Supporting Information

## **Experimental details**

**Materials.** Platinum (Pt) sputtering target (1.00" dia. x 0.063" thick, 99.99% purity), Copper (Cu) evaporation pellets (1/4" dia. x 1/2" length, 99.999% purity) and Nickel (Ni) evaporation pellets (1/4" dia. x 1/2" length, 99.995% purity) were purchased from Kurt J. Lesker. Acetone (ACS reagent, 99.5%) was purchased from Sigma-Aldrich and sodium hydroxide (NaOH, 96.7%) was purchased from Macron Chemicals.

**Thin-film deposition.** Thin metal films of Pt, Cu and Ni were deposited by a Modular Thin Film Deposition System (Lesker 18) by sputtering and electron beam deposition on PMMA substrates (base vacuum  $5 \times 10^{-6}$  Torr), at deposition rates of 0.9 Å/s to 1.2 Å/s. The thickness of all films in this study was 20 nm, which was controlled by a thickness monitor.

**Characterization of the deposited thin films.** Surface mapping was measured by Zygo optical surface profiler capable of measuring feature heights ranging from < 2 nm up to 20000 μm, it was found that all the deposited thin films display homogeneous surfaces. X-ray diffraction (Bruker D8 Discover using monochromatic Cu K $\alpha$  radiation at 40 KV and 40 mA) was carried

out on the deposited thin films (Figure S1). No measurable changes in the diffraction patterns were seen after strain cycling.

***Electrochemical measurements.*** Electrochemical studies were carried out in a standard three electrode system controlled by a Metro (Autolab PGSTAT 30) electrochemistry workstation. In all experiments, an Ag/AgCl reference electrode was employed and Pt coiled wire was used as the counter electrode. 0.1 M NaOH solution was used as the electrolyte, which was prepared by dissolving the calculated amount of NaOH with the conductivity of 0.056 s/m water (at 25 °C) to form 0.1 M solution. The electrolyte was sparged with ultra-high purity argon (99.999%); all potentials reported in this paper are converted to the pH-independent reversible hydrogen electrode (RHE) scale. All experiments were repeated three times to confirm reproducibility. The electrochemical measurements were conducted in a three-electrode cell which was fabricated to be integrated with an Instron 4505 universal mechanical testing machine; the experimental setup is illustrated in Figure 1 of the main text. The design and the connection of the as-obtained metal film as working electrode are shown in Figure S3. This setup allows *in-situ* measurements of electrochemical responses while the specimen is under uniaxial tension and compression. The scan rate of all electrochemical measurements was 50 mV/sec.

The cell was constructed such that the electrolyte-gas interface defined the top of the active electrochemical area; in this way, the geometric differences between active catalyst area in strained and unstrained cases were minimized. To simplify the analysis, we normalized all geometric current densities by the unstrained value (which further implicitly assumes that the number of active sites did not change with strain). Here, we examine the sensitivity of our results to this assumption, using data from case of Pt in unstrained versus at 0.4% nominal strain and comparing three different geometry assumptions. Our unstrained electrode height ( $L_1$ ) was

approximately 25 mm and its width ( $W_1$ ) was approximately 6.5 mm. Therefore, its unstrained area was  $A_1 = L_1W_1 = 162.5 \text{ mm}^2$ , which by our working assumption (Assumption #1) was used to normalize the current for all strain cases. At our maximum reported loading of +0.4%, we can first (Assumption #2) calculate that the height expands to  $L_2 = 25.1 \text{ mm}$  (0.4% elongation), and the width will shrink by the Poisson ratio of the PMMA substrate (0.38) to  $W_2 = 6.5 \times (1 - 0.004 \times 0.38) = 6.49 \text{ mm}$ . Under the assumption that both these dimensional changes lead to a change in catalytic area, this leads to  $A_2 = L_2W_2 = 162.9 \text{ mm}^2$ . Under another scenario (Assumption #3), which matches the physical description most closely, we assume that the experimental setup results in the length being unchanged as the top edge of the electrocatalyst is defined by the electrolyte-gas interface. Therefore, in this scenario  $L_3 = L_1 = 25 \text{ mm}$  and  $W_3 = W_2$ ; therefore,  $A_3 = L_3W_3 = 162.25 \text{ mm}^2$ . Choosing a typical point on the CV of -0.166 V, we recorded a current density at 0% loading of  $-0.899 \text{ mA/cm}^2$ . For the case of +0.4% nominal strain, under Assumptions #1, #2, and #3, respectively, the strained current density would be reported as  $-0.871$ ,  $-0.869$ , and  $-0.872 \text{ mA/cm}^2$ . That is, all three assumptions lead to  $-0.87 \text{ mA/cm}^2$  when reported to the two significant digits to which we have confidence, as opposed to  $-0.90 \text{ mA/cm}^2$  for the unstrained case. To a good approximation, we are insensitive to the method of normalizing area (for the case of these rather small strains), and thus we choose the simplest case of Assumption #1 in this study.

***Voltage change measurements.*** In order to measure the potential shift due to strain, the difference between the reduction portion of the CVs corresponding to the strained and unstrained cases was obtained in a suitable current density range. The current density range was chosen such that the response was purely Faradaic in nature (corresponding to  $\text{H}_2$  evolution electrocatalysis) as opposed to capacitive current. This was identified by the region of the CV in

which the reductive (negative-going) and oxidative (positive-going) sweeps overlapped, rather than exhibiting hysteresis characteristic of a capacitive process. We chose this region first for the Pt catalyst, then for consistency chose the same distance from the visible “knee” on the CV of approximately -0.07 V. This strategy was employed to minimize capacitive effects; to attempt to minimize convolutions from mass transport, we chose the potential window we studied to be small (approximately 40 mV) to avoid extending the analysis into regions of large current density. However, in practice the curves exhibited the same shift also at the more negative potentials. Further information on the geometry of the cell is described above. For the case of Pt,  $\Delta V$  was measured in the current density range of -0.7 to -0.3 mA/cm<sup>2</sup> at increments of 0.025 mA/cm<sup>2</sup> and the average of these values is taken as the potential shift for the corresponding applied strain. The corresponding current density ranges for Ni and Cu are -2.25 to -1.0 mA/cm<sup>2</sup> and -0.175 to -0.0375 mA/cm<sup>2</sup>, respectively. The error bars shown in Figure 3 include the spread in the  $\Delta V$  variation within the current range described above, as well as the sample-to-sample variation.

### **Computational methodology**

The hydrogen evolution reaction was examined over Pt, Ni, and Cu(111) surfaces under application of an in-plane uniaxial strain. Each surface was constructed using a  $2 \times 2$  unit cell with four layers and 20 Å vacuum employing the corresponding DFT bulk lattice constants. Introducing more metal layers is assumed to not change adsorption energies significantly, as has been previously investigated by Mavrikakis *et al.*<sup>[1]</sup> and Skúlason *et al.*<sup>[2]</sup>, and trends (differences) in binding energies can be expected to converge faster than the binding energies themselves.<sup>[3]</sup> Strain applied in one direction leads to a relaxation in the other two orthogonal directions. By assuming that the thin metal film experiences the same in-plane mechanical

deformation as that of substrate, the amount of transverse relaxation was calculated from Poisson's ratio of the PMMA substrate, and was explicitly included while constructing the surface unit cell. The top three layers in the unit cell (and the adsorbates) were allowed to relax, forcing the bottom layer to the spacing of the bulk crystal (at appropriate strain). The exposed facet was not assumed to have a bias to its alignment with respect to the strain; that is, it is assumed to have uniformly random distribution of lattice directions. This assumption is reflected in the model by taking the average of the two cases in which the uniaxial strain was applied along the  $x$ - and  $y$ - directions of the unit cell; convention for  $x$ - and  $y$ - axes of the unit cell is adopted according to Figure 4a (shown by blue color) of the manuscript, with the  $z$ -direction being normal to [111] surface.

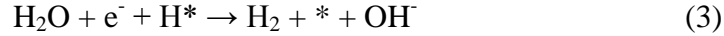
All density functional theory (DFT) calculations were performed using the planewave DACAPO electronic structure code with ionic manipulations in the Atomic Simulation Environment (ASE) <sup>[4]</sup>, converging Kohn-Sham iterations to within a  $10^{-5}$  eV variation in energy as well as  $10^{-4}$  and  $10^{-3}$  variations in density and occupation of states, respectively. To improve electronic convergence, the occupation of Kohn-Sham states was smeared according to a Fermi-Dirac distribution with a thermal energy  $k_B T = 0.1$  eV, with standard extrapolation of electronic energies to  $k_B T = 0$  eV before the application of statistical-mechanical temperature effects, described below. Electronic wave functions were expanded in a plane-wave basis set, and inner electrons were represented by Vanderbilt ultrasoft pseudopotentials. <sup>[5,6]</sup> In order to ensure the obtainment of converged results, fairly large values of 450 eV and 500 eV were used for the plane-wave cut-off and density cut-off, respectively. To approximate the exchange and correlation of electrons, the revised Perdew-Burke-Ernzerhof (RPBE) density functional of Hammer, Hansen, and Nørskov has been used, which was developed to be more accurate than

PBE for the calculation of binding energies of adsorbates on transition-metal surfaces <sup>[7]</sup>. For the cases of Pt and Ni, the Brillouin zone integration was carried out using a  $4 \times 4 \times 1$  Monkhorst-Pack  $k$ -point grid for a system of  $2 \times 2$  atoms in the unit cell <sup>[2, 8]</sup>. For the case of Cu, however, a finer  $k$ -point grid was necessary for the obtainment of converged energies, as has been also pointed out by Sakong and Groß <sup>[9]</sup>; here we used  $10 \times 10 \times 2$ . In order to cancel out the net surface dipole density, standard dipole corrections were included at the farthest point in the vacuum in our calculations as implemented in the DACAPO calculator. In the case of Ni, spin polarization was taken into account; all other calculations were taken as spin-paired.

It is widely assumed that HER proceeds via the following mechanism in alkaline medium:



Alternatively the second step can be:



Similar to HER mechanism in acidic medium, the main entity in the above steps is the H adsorbed species,  $\text{H}^*$ . Therefore, the free energies for H adsorption ( $\Delta G_{\text{H}}$ ) can be used as a primary descriptor of HER activity.  $\Delta G_{\text{H}}$  at 298 K is calculated via the computational hydrogen electrode (CHE) model <sup>[3]</sup> as:

$$\Delta G_{\text{H}}(\theta_{\text{H}}) = \Delta E_{\text{H}}(\theta_{\text{H}}) + \Delta E_{\text{ZPE}} - T\Delta S_{\text{H}} + \Delta G_{\text{V}} \quad (4)$$

where  $\Delta E_{\text{H}}(\theta_{\text{H}})$  is the differential hydrogen adsorption energy:

$$\Delta E_{\text{H}}(\theta_{\text{H}}) = E(n\text{H}^*) - E((n-1)\text{H}^*) - \frac{1}{2} E(\text{H}_2) \quad (5)$$

In Eq. (5),  $n = 1-4$  H atoms as coverage increases from 0.25 to 1.0 monolayer (ML). A pH correction to  $\Delta G_{\text{H}}(\theta_{\text{H}})$  is not invoked as the reference is the reversible hydrogen electrode (RHE). The correction for the electrical potential  $\Delta G_{\text{V}} = -e V$ , where  $e$  is the (positive) charge of

an electron (Faraday's constant divided by Avogadro's number) and  $V$  is the potential relative to 0 V RHE. We note that the CHE model considers only the energetics of the stable elementary thermodynamic states (adsorbed hydrogen), and not barriers between them. However, barriers are assumed to follow linear free-energy relations with respect to endstate energetics, and thus the simple voltage shifts implied by the CHE model can be expected to correlate with experimental measurements. The zero-point energy of an atomic configuration can be obtained from a normal-mode vibration analysis according to  $E_{ZPE} = \frac{h}{2} \sum_i^{\text{DOF}} \nu_i$ , where the summation runs over the vibrational degrees of freedom in the system. When a hydrogen atom is adsorbed to the surface, we assume that the frequencies of vibration of the metal atoms of the slab are not affected by the adsorbed hydrogen. Therefore, when calculating the difference between zero-point energies of the system before and after hydrogen adsorption, the terms corresponding to frequencies of vibration of slab atoms cancel out, and we have

$$\Delta E_{ZPE} = 0.5h \left( \sum_{i=1}^{3n} \nu_i - \sum_{j=1}^{3(n-1)} \nu_j - \nu_0 \right) \quad (5)$$

where  $\nu_i$  is the frequency of vibration of  $n$  adsorbates,  $\nu_j$  is the frequency of vibrations of  $n - 1$  adsorbates, and  $\nu_0$  is the frequency of stretch of hydrogen molecule (calculated here as 3291.3  $\text{cm}^{-1}$ ). After frequencies of vibration are found, entropy of a canonical ensemble can be calculated from

$$\frac{S(T)}{N} = k_B \sum_{i=1}^{3n} \left( \frac{h\nu_i}{k_B T (e^{h\nu_i/k_B T} - 1)} - \ln(1 - e^{-h\nu_i/k_B T}) \right) \quad (6)$$

When calculating differential entropy change  $\Delta S_H$ , the entropy of gas-phase hydrogen atom was assumed as  $S_H = \frac{1}{2} S_{H_2} = 6.77 * 10^{-4}$  eV/K, the entropy of gas-phase hydrogen at room temperature. We have further assumed that entropy and zero-point energy contributions stay the

same for different values of strain, and therefore they have been calculated for zero-strain cases only.

Hydrogen adsorption was considered at the most favored adsorption sites. For H coverages ( $\theta_H$ ) of 0.25, 0.75, and 1.0 ML (monolayer, where 1 ML corresponds to 1 H atom per surface metal atom), these are *fcc* sites<sup>[8, 10]</sup>, which we confirmed in the current study. For an H coverage of 0.5 ML, we found the lowest energy configuration on Pt to be with all hydrogen atoms at *fcc* sites, but for Ni and Cu surfaces with half of the hydrogen atoms at *fcc* sites and the other half at *hcp* sites (as reported in the literature for Ni<sup>[11]</sup>), which was taken into account in the calculations. To estimate the reactive hydrogen coverage ( $\theta_H$ ), we started with the experimental work of Markovic *et al.*<sup>[10]</sup> where adsorption isotherms of underpotential deposition of H on Pt(111) in 0.05 M H<sub>2</sub>SO<sub>4</sub> relating  $\theta_H$  to potential are reported. According to their study, at a temperature of 303 K,  $\theta_H$  of 0.25 and 0.68 ML occurs at RHE potential ( $U$ ) of about 0.23 and 0 V, respectively. In a subsequent DFT study, Skúlason *et al.*<sup>[2]</sup> predicted that a low  $\theta_H$  of 0.25 ML on Pt(111) corresponds to a moderate positive potential of  $U = +0.18$  V. When a full monolayer of hydrogen was formed,  $U$  was close to zero. Therefore, in our DFT study, we considered  $\theta_H$  of 0.5 and 0.75 ML for Pt(111). Moreover, our calculated binding energies of a single hydrogen atom on unstrained M(111) show that hydrogen adsorption is much stronger on Ni and considerably weaker on Cu as compared to Pt. Therefore, in the proceeding analysis, we assumed that at  $U = 0$  V, hydrogen coverage over Ni and Cu would be, respectively, higher and lower than Pt, leading to assuming  $\theta_H = 1$  ML for Ni (as has been also reported by the reference [10]) and  $\theta_H = 0.25$  and 0.5 for Cu.

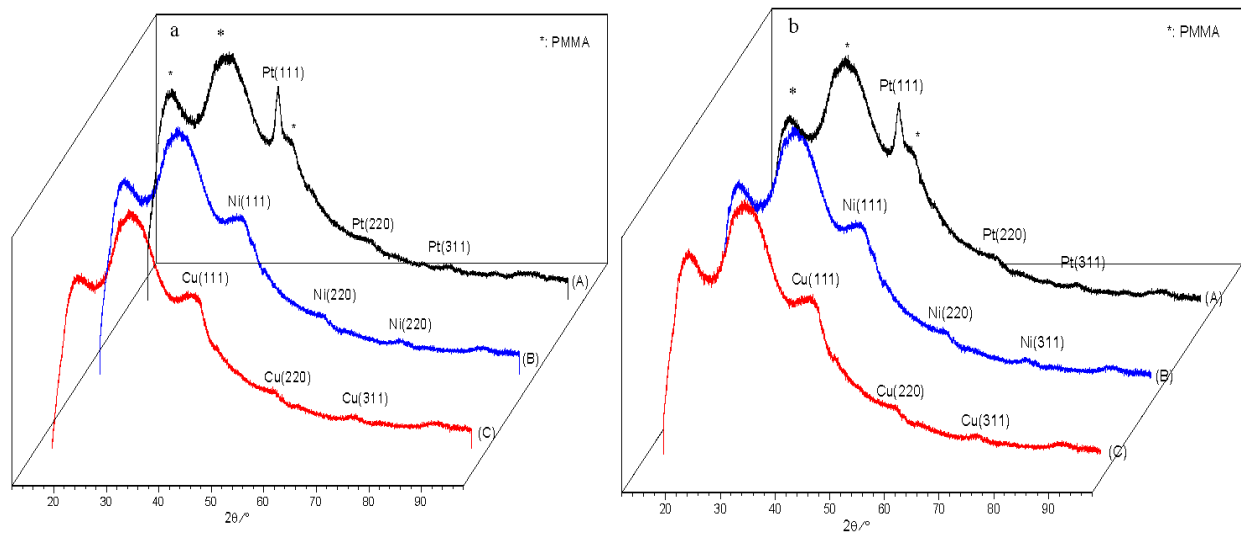


**Figure S1.** XRD patterns of the fresh (a) and spent (b) metal thin films. The XRD patterns before and after the experiment were nearly identical, with no measurable changes in the film texture.

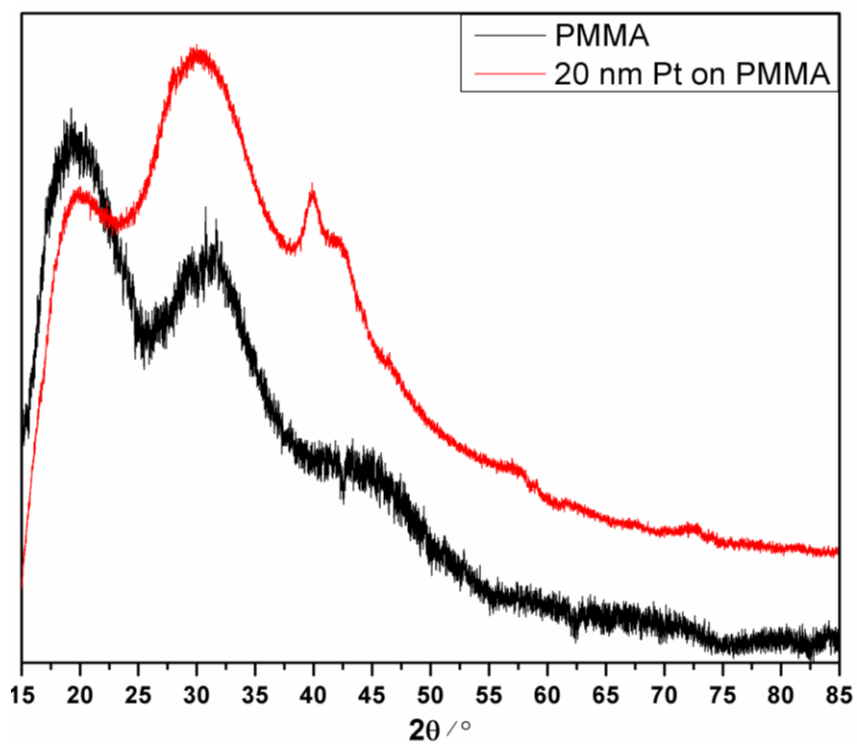


**Figure S2.** The diffraction pattern of PMMA substrate and the as-obtained 20 nm Pt films on PMMA substrate.

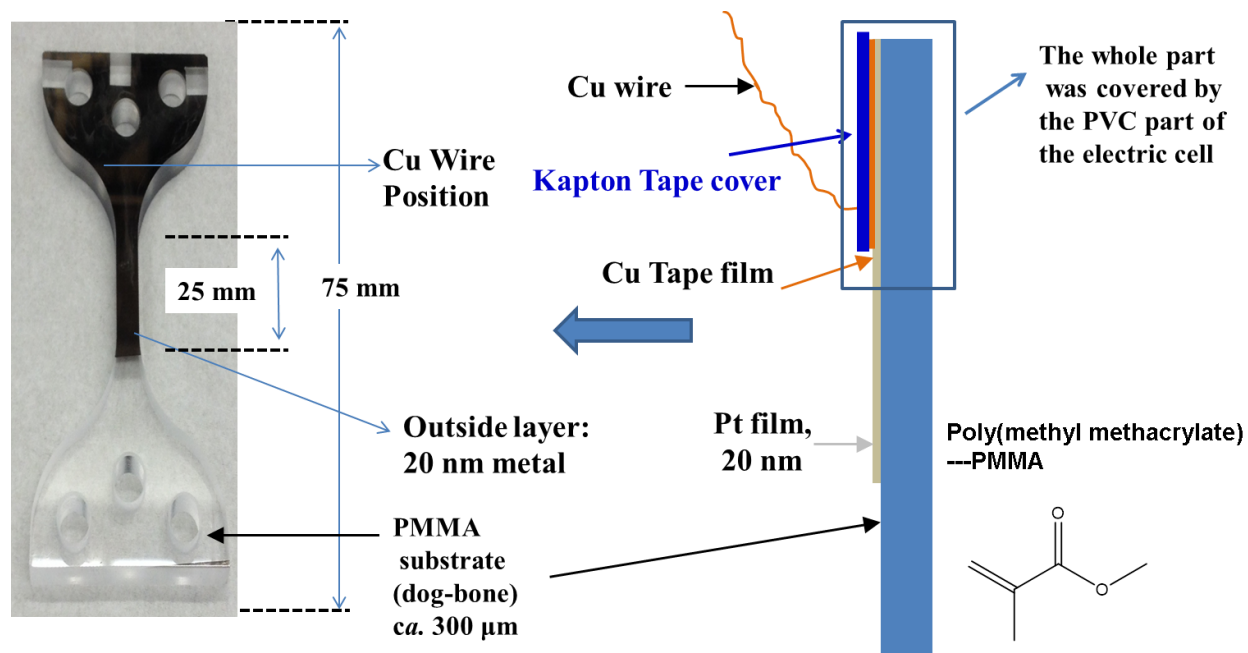


**Figure S3.** The assemble and contact of metal films as the working electrode.

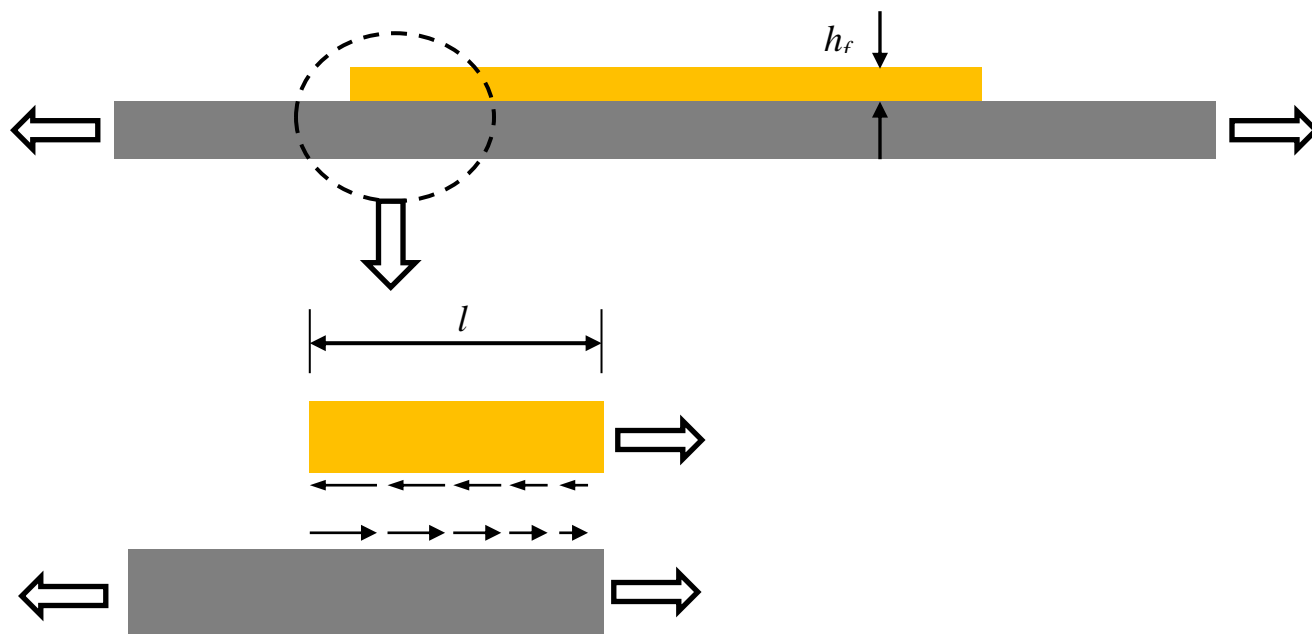


**Figure S4.** (top) Schematic illustration of a film bonded on a substrate, which is subjected to in-plane loading and elastic strain as shown. (bottom) Magnified view of the film edge, in which the arrows represent the shear stress that is induced along the interface. The length of the arrows represents the shear stress magnitude; note that the magnitude of the shear stress approaches zero over a distance  $l$  from the film edge. Note that in-plane stress in the film at the left edge is zero

(it is a free-surface). However, as the as we move away from the edge, normal stress develops in the film, which is necessary to maintain equilibrium by counteracting the interfacial shear stress. At a distance  $l$  from the edge, the shear stress approaches zero and the in-plane stress in the film reaches a steady state value, which corresponds to the elastic strain in the substrate.<sup>[12]</sup>

### Strain transfer

Subjecting films to tensile or compressive stress by straining the substrates on which they are deposited is a common and widely used technique.<sup>[13-19]</sup> For an elastic film on an elastic substrate, when the substrate is strained, the film inherits the substrate strain beyond a transition length  $l$  from its edge, as shown above. So, except in these transition regions, the film strain is equal to that of the substrate.<sup>[12]</sup> The transition length  $l$  can be estimated from previous works.<sup>[20]</sup>

$$l \sim 10 h_f/k$$

where

$$k = \frac{E_s}{1 - \nu_s} \frac{1 - \nu_f}{E_f}$$

$E_s$  and  $E_f$  are the Young's moduli of the substrate and the film respectively;  $\nu_s$  and  $\nu_f$  are the Poisson's ratios of the substrate and the film respectively. For the combination of PMMA substrate and metal films,  $k \sim 1/100$ , hence  $l \sim 1000 h_f$ . In our experiments,  $h_f \sim 20$  nm, which results in a transition length of  $l \sim 20$   $\mu$ m, which is negligible compared to the in-plane dimensions of the film of about 6.5 mm x 25 mm. Since the area of the transition zone is a negligible fraction of the total film area, the entire film can be considered to be under the same elastic strain as that of the substrate.

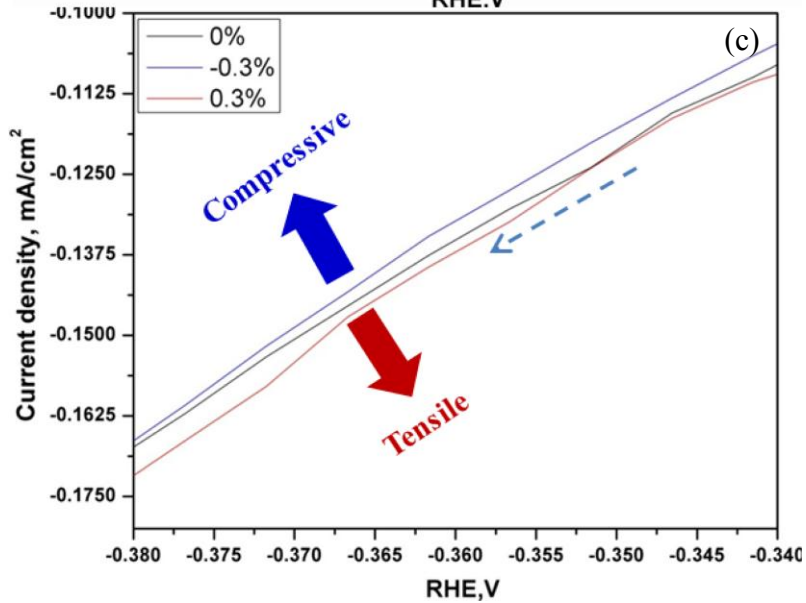
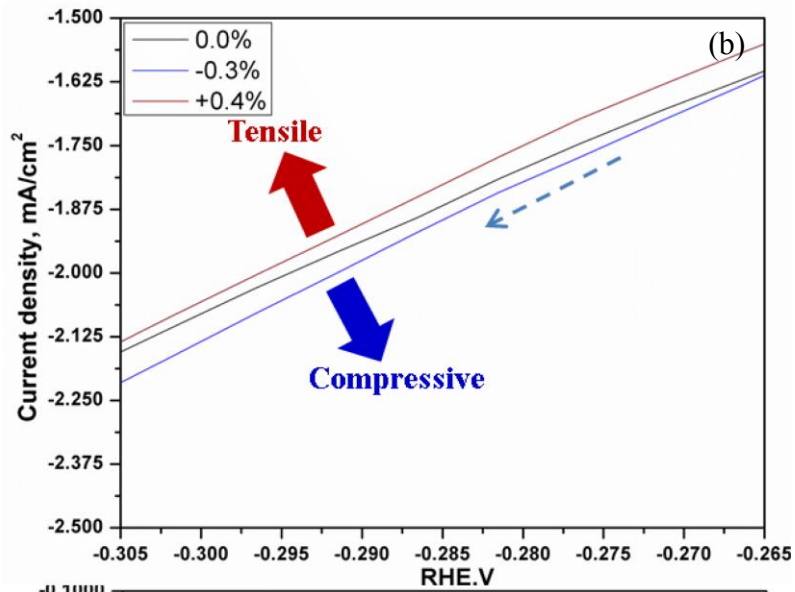
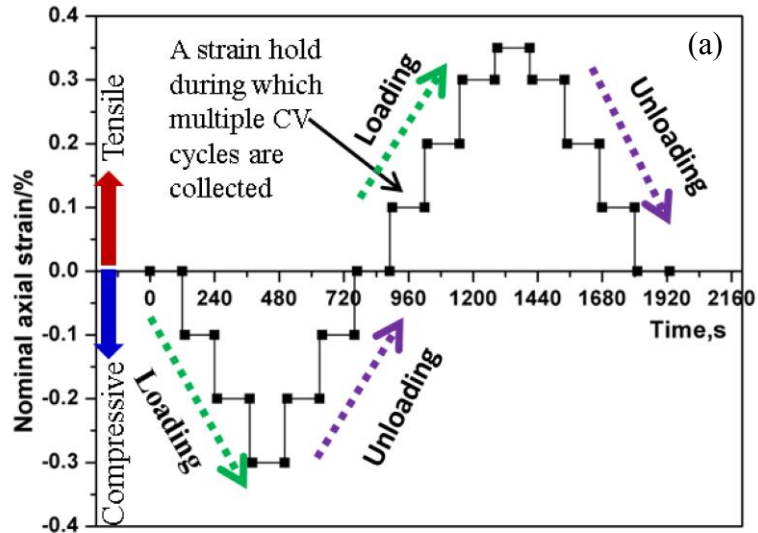


**Figure S5.** (a) Schematic illustration of the loading history on the PMMA substrates, showing progressively increasing compressive and tensile strains. (b) Magnified view of Ni thin film in the HER region showing only the reduction sweep at 3 different strain values. (c) Magnified view of Cu thin film in the HER region showing only the reduction sweep at 3 different strain values. Note the systematic shift in the CV curves with strain.

## References

- [1] M. Mavrikakis, B. Hammer, J. K. Nørskov, *Phys. Rev. Lett.* **1998**, *81*, 2819.
- [2] E. Skúlason, G. S. Karlberg, J. Rossmeisl, T. Bligaard, J. Greeley, H. Jónsson, J. K. Nørskov, *Phys. Chem. Chem. Phys.* **2007**, *9*(25), 3241-3250.
- [3] A. J. Medford, J. Wellendorff, A. Vojvodic, F. Studt, F. Abild-Pedersen, K. W. Jacobsen, T. Bligaard, J. K. Nørskov, *Science*, **2014**, *345*, 197-200.
- [4] S. R. Bahn, K. W. Jacobsen, *Comput. Sci. Eng.* **2002**, *4*, 56-66.
- [5] D. Vanderbilt, *Phys. Rev. B* **1990**, *41*, 7892-7895.
- [6] J. K. Nørskov, J. Rossmeisl, A. Logadottir, L. Lindqvist, J. R. Kitchin, T. Bligaard, H. Jónsson, *J. Phys. Chem. B* **2004**, *108*, 17886–17892.
- [7] B. Hammer, L. B. Hansen, J. K. Nørskov. *Phys. Rev. B* **1999**, *59*, 7413.
- [8] T. A. Maark, A. Peterson, *J. Phys. Chem. C* **2014**, *118*, 4275-4281.
- [9] S. Sakong, A. Groß, *Surf. Sci.* **2003**, *525*, 107-118.
- [10] N. M. Marković, B. N. Grgur, P. N. Ross, *J. Phys. Chem. B* **1997**, *101*, 5405-5413.
- [11] J. Greeley, M. Mavrikakis, *Surf. Sci.* **2003**, *540* (2), 215-229.
- [12] L. B. Freund, S. Suresh, *Thin film materials: stress, defect formation and surface evolution*. Cambridge University Press, **2004**, P223-237.
- [13] N. Lu, X. Wang, Z. Suo, J. Vlassak, *Appl. Phys. Lett.* **2007**, *91*(22), 221909.
- [14] H. J. Jin, J. Weissmüller, *Science*, **2011**, *332*(6034), 1179-1182.

- [15] M. Smetanin, Q. Deng, J. Weissmüller, *Phys. Chem. Chem. Phys.* **2011**, *13*(38), 17313-17322.
- [16] Q. Deng, M. Smetanin, J. Weissmüller, *J. Catal.* **2014**, *309*, 351-361.
- [17] M. Smetanin, D. Kramer, S. Mohanan, U. Herr, J. Weissmüller, *Phys. Chem. Chem. Phys.* **2009**, *11*(40), 9008-9012.
- [18] J. Lohmiller, R. Baumbusch, O. Kraft, P. A. Gruber, *Phys. Rev. Lett.* **2013**, *110*(6), 066101.
- [19] Y. Yang, T. A. Maark, A. Peterson, S. Kumar, *Phys. Chem. Chem. Phys.* **2015**, *17*, 1746-1754.
- [20] L. B. Freund, S. Suresh, *Thin film materials: stress, defect formation and surface evolution*. Cambridge University Press, **2004**, P225.